1 **Continental pollution in the Western Mediterranean basin: large variability of**

2 **the aerosol single scattering albedo and influence on the direct shortwave**

3 **radiative effect**

4 Claudia Di Biagio[1], Paola Formenti[1], Lionel Doppler[2], Cécile Gaimoz[1], Noel Grand[1], Gerard

5 Ancellet[3], Jean-Luc Attié[4,5], Silvia Bucci[6,7], Philippe Dubuisson[8], Federico Fierli[6], Marc

6 Mallet[5], and François Ravetta[3]

7 *[1] LISA, UMR CNRS 7583, Université Paris Est Créteil et Université Paris Diderot, Institut Pierre*
8 *Simon Laplace, Créteil, France*

9 *[2] Deutscher Wetterdienst, Metorological Observatory Lindenberg, Germany*

10 *[3] Sorbonne Universités, UPMC Univ. Paris 06; Université Versailles St-Quentin; CNRS/INSU,*
11 *LATMOS-IPSL, Paris, France*

12 *[4] Laboratoire d'Aérologie, University of Toulouse, UMR 5560 CNRS, France*

13 *[5] CNRM UMR 3589, Météo-France/CNRS, Toulouse, France*

14 *[6] Institute for Atmospheric Sciences and Climate of the National Research Council , (ISAC-CNR),*
15 *Rome, 00133, Italy*

16 *[7] Sc. Dept. of Physics, Ferrara University, Ferrara, 44121, Italy*

17 *[8] Laboratoire d'Optique Atmosphérique, Université Lille, Villeneuve d'Ascq, 59655 Cedex, France*

20 Correspondence to:

21 C. Di Biagio (claudia.dibiagio@lisa.u-pec.fr) and P. Formenti (paola.formenti@lisa.u-pec.fr)

34 **Abstract**

35 Pollution aerosols strongly influence the composition of the Western Mediterranean basin,

36 but at present little is known on their optical properties. We report in this study in situ

37 observations of the single scattering albedo (ω) of pollution aerosol plumes measured over

38 the Western Mediterranean basin during the TRAQA (TRansport and Air QuAlity) airborne

39 campaign in summer 2012. Cases of pollution export from different source regions around

40 the basin and at different altitudes between ~160 and 3500 m above sea level were sampled

41 during the flights. Data from this study show a large variability of ω, with values between

42 0.84-0.98 at 370 nm and 0.70-0.99 at 950 nm. The single scattering albedo generally

43 decreases with the wavelength, with some exception associated to the mixing of pollution

44 with sea spray or dust particles over the sea surface. The lowest values of ω (0.84-0.70

45 between 370 and 950 nm) are measured in correspondence of a fresh plume possibly linked

46 to ship emissions over the basin. The range of variability of ω observed in this study seems to

47 be independent of the source region around the basin, as well as of the altitude and aging time

48 of the plumes. The observed variability of ω reflects in a large variability for the complex

49 refractive index of pollution aerosols, which is estimated to span in the large range 1.41-1.75

50 and 0.002-0.068 for the real and the imaginary parts, respectively, between 370 and 950 nm.

51 Radiative calculations in clear-sky conditions were performed with the GAME radiative

52 transfer model to test the sensitivity of the aerosol shortwave Direct Radiative Effect (DRE)

53 to the variability of ω as observed in this study. Results from the calculations suggest up to a

54 50% and 30% change of the forcing efficiency (FE), i.e. the DRE per unit of optical depth, at

55 the surface ($-160 \div -235$ Wm$^{-2}\tau^{-1}$ at 60° solar zenith angle) and at the Top-Of-Atmosphere ($-$

56 $137 \div -92$ Wm$^{-2}\tau^{-1}$) for ω varying between its maximum and minimum value. This induces a

57 change of up to an order of magnitude ($+23 \div +143$ Wm$^{-2}\tau^{-1}$) for the radiative effect within the

58 atmosphere.

59

60

61 **Keywords**: pollution aerosols, single scattering albedo, direct radiative effect, Western

62 Mediterranean

63

64

65

1. **Introduction**

Atmospheric aerosols play a crucial role on climate by affecting the radiative transfer of atmospheric radiation and by modifying cloud properties and lifetime (Boucher et al., 2013). The capability of atmospheric aerosols to interact through processes of scattering and absorption with the atmospheric radiation, so to exert a direct radiative effect (DRE), depends on their spectral optical properties (extinction efficiency, k_{ext}, single scattering albedo, ω, and asymmetry factor, g). In particular the single scattering albedo has been demonstrated to be a key parameter in modulating the surface, Top-of-Atmosphere (TOA), and atmospheric aerosol DRE (e.g., Ramana and Ramanathan, 2006; Di Biagio et al., 2010; Loeb and Su, 2010). Aerosol optical properties can largely vary depending on the particles composition, size distribution, and shape, which are function of the aerosol source, type, and processing occurring during atmospheric lifetime. At present, the capability of climate models in reproducing all the possible heterogeneity in aerosol optical properties represents the main source of uncertainty in evaluating their DRE on climate (McComiskey et al., 2008; Stier et al., 2013). In this sense, intensive studies providing the characterization of the aerosol optical properties and their local and regional variability are of great importance in order to reduce these uncertainties.

This is particularly the case of the Western Mediterranean basin. Indeed, the Mediterranean is a very complex region, characterized by the presence of air masses carrying aerosols of different origins and types (Gkikas et al., 2012). On its northern bound, it is limited by Europe, with a consequent frequent export of anthropogenic pollution from the continent towards the basin (Lelieveld et al., 2002; Pace et al., 2006). In particular, the Western part of the Mediterranean basin, surrounded by large coastal megacities, commercial harbours, and under the direct influence of some of the most industrialized areas of the continent (such as the Po Valley in Northern Italy or the Fos/Berre area in Southern France), is strongly affected by continental pollution outflows (Pérez et al., 2008; Pey et al., 2010; Di Biagio et al., 2015). The build-up of high pollution levels over the Western basin is particularly favoured during summer when the strong insolation enhances photochemical reactions and the stable meteorological conditions promote the stagnation of pollutants (Millan et al., 2000; Mallet et al., 2005).

In spite of this, the characterization of the optical properties of anthropogenic aerosols in this part of the basin remains only limited to coastal and inland regions (Mallet et al., 2003, 2011, 2013; Lyamani et al., 2006; Estelles et al., 2007; Saha et al., 2008; Esteve et al., 2012;

99   Piazzola et al., 2012; Pandolfi et al., 2011 and 2014), or remote islands actually far from the

100   strong influence of continental outflows (Lyamani et al., 2015). Moreover, the majority of

101   these studies uses remote sensing measurements and analyse aerosol properties integrated

102   over the entire atmospheric column, without information on their vertical variability. Thus, at

103   present, we miss a detailed characterization of the optical properties of the pollution aerosol

104   over the entire region, in particular over the remote sea, and its vertical distribution.

105   To fill this gap, the international ChArMEx (Chemistry-Aerosol Mediterranean Experiment;

106   http://charmex.lsce.ipsl.fr) research program has supported in recent years two airborne

107   campaigns over the Western Mediterranean basin: TRAQA (Transport and Air QuAlity) in

108   2012 and SAFMED (Secondary Aerosol Formation in the MEDiterranean) in 2013.

109   In a recent paper, Di Biagio et al. (2015) have presented in situ measurements of the aerosol

110   vertical profiles acquired over the remote sea during these campaigns. Observations from

111   TRAQA and SAFMED have shown that in the Western basin pollution plumes extend as far

112   as hundreds of km from the coastline and reach up to ~4000 m, presenting a complex

113   stratified structure, and pollution plumes show a large heterogeneity in terms of composition,

114   origin, and lifetime.

115   Following these observations, we may ask: does the heterogeneity in pollution plume

116   composition, origin, and lifetime as observed in Di Biagio et al. (2015) induce heterogeneity

117   on the optical properties (in particular the single scattering albedo) of pollution aerosols in

118   this part of the basin? And, if observed, does this heterogeneity on the optical properties

119   influence the aerosol DRE? Is it necessary to take it into account to better evaluate the aerosol

120   radiative impact in the Western Mediterranean?

121   With the aim of answering these questions, in this paper we analyse data of the optical

122   properties (spectral scattering and absorption coefficients, single scattering albedo) and size

123   distributions of pollution aerosols measured over the Western Mediterranean basin during

124   TRAQA. SAFMED observations have been excluded here given that only limited data on the

125   aerosol optical properties were available from this campaign. The objective of the paper is

126   twofold: to provide a new dataset of aerosol single scattering albedo values which can be

127   representative of the polluted aerosols over the Western basin, and investigate the sensitivity

128   of the aerosol direct DRE to the variability of this parameter.

129

130

131

2. Overview of flights during the TRAQA campaign

The TRAQA campaign took place in the period 20 June – 13 July 2012. Instruments were installed on board the SAFIRE (Service des Avions Français Instruments pour la Recherche en Environnement, http://www.safire.fr/) tropospheric aircraft ATR-42, based in Toulouse (43° 36' N, 1° 26' E, France). A total of seventeen flights, most often two flights per day, with intermediate stops in different airports in southern France and Corsica, were performed (flight numbers V16 to V32). The majority of flights were over the sea, with some exceptions investigating inland areas in southern France. The flight altitude for the ATR-42 ranged between a minimum of ~60 m to a maximum of ~5000 m above sea level (a.s.l.), and the maximum flight time was 4 h. The general flight strategy consisted of legs at constant altitude to sound the vertical structure by lidar observations, vertical ascents/descents to describe the vertical atmospheric column and identify the main aerosol plumes, followed by straight levelled runs (SLRs) within the detected aerosol layers. In the present study we will exclusively consider measurements acquired during SLRs, since only during these phases the whole set of aerosol optical properties (scattering and absorption coefficients) were measured. A total of 21 SLRs were performed over the sea surface or inland close to the coastline and will be considered in this study. Figure 1 and Table 1 summarise the geographical location, date, time, and altitude of these 21 SLRs. As indicated in Table 1 each SLR was about 15-20 min long. At the cruise speed of the ATR (93 ms^{-1}), this integration time corresponds to about 100 km.

3. Measurements and methods

3.1 Aircraft observations

Aerosol sampling on the ATR-42 was performed using the AVIRAD system. AVIRAD is an iso-axial and iso-kinetic inlet which samples air at a volumetric flow of ~350 L min^{-1}. The 50% passing efficiency of the inlet is 12 μm diameter. Various lines depart from AVIRAD to connect to different instruments for the measurement of the aerosol physico-chemical and optical properties. Additionally, several sensors for the measurements of the atmospheric composition were installed on the ATR-42 aircraft as basic equipment. A brief description of the different in situ measurements considered in this study from the AVIRAD system and the ATR-42 equipment and their data analysis is reported in the following.

- The aerosol scattering coefficient (σ_s) at 450, 550, and 700 nm was measured by a 3-wavelength integrating nephelometer (TSI Inc., model 3563, 6s resolution). The

165 nephelometer was calibrated prior the campaign by using air and CO_2 as reference gases.

166 Nephelometer measurements were corrected for angular truncation and Lambertian non-

167 idealities by applying the formula by Anderson and Ogren (1998), appropriated to

168 submicron aerosols which we expected in the pollution plumes sampled during the

169 campaign. The measurement uncertainty on σ_s, calculated taking into account for the

170 photon counting, gas calibration, and angular corrections uncertainties, was estimated to

171 be lower than 10% at the three wavelengths. Averages of the scattering coefficient were

172 calculated over the different SLRs. The uncertainty on the SLR average values was

173 estimated as the combination of the measurement uncertainty and the standard deviation

174 along each individual run. For each SLR, the particle scattering Ångström exponent (SAE)

175 was calculated as the power law fit of the measured scattering coefficients versus

176 wavelength to extrapolate the scattering coefficient at other wavelengths than those of

177 operation.

178 The nephelometer measured the scattering coefficient in dry air conditions. This is due to

179 the heating of the airflow while entering the aircraft cabin and the temperature increase in

180 the sensing volume of the instrument due to illumination. The relative humidity measured

181 during the flights inside the nephelometer cavity was <25% in more than 90% of cases,

182 with values up to ~40% occasionally observed <200 m over the sea surface.

183 - The aerosol absorption coefficient (σ_{abs}) at 370, 470, 520, 590, 660, 880, and 950 nm was

184 measured by a 7-wavelength aethalometer (Magee Sci., model AE31, 2min resolution).

185 The principle of operation of the aethalometer consists in measuring the attenuation of

186 light through an aerosol-laden filter compared to that of another portion of the filter which

187 is unexposed to the air flow and is used as a reference (Weingartner et al., 2003). To yield

188 the aerosol absorption coefficient, the spectral attenuation $\sigma_{ATT}(\lambda)$ measured by the

189 aethalometer was corrected following the procedure described by Collaud Coen et al.

190 (2010):

191 $$\sigma_{abs}(\lambda) = \frac{\sigma_{ATT}(\lambda) - \alpha(\lambda)\overline{\sigma_s(\lambda)}}{C_{ref}R(\lambda)} \qquad (1).$$

192 The different terms in equation 1 are: (i) $\alpha(\lambda)\overline{\sigma_s(\lambda)}$ or "scattering correction". In this work

193 $\alpha(\lambda)$ was calculated with the formula by Arnott et al. (2005) and varied between 0.02 and

194 0.07, while $\overline{\sigma_s(\lambda)}$ was the average of the scattering coefficient along the considered SLR

195 extrapolated at the aethalometer wavelengths; (ii) C_{ref} or "multiple scattering correction".

196   C_{ref} was set to 2.14 ± 0.21 (wavelength-independent) following Weingartner et al. (2003);

197   (iii) $R(\lambda)$ or "shadowing effect correction". $R(\lambda)$ depends on the charge and

198   absorptivity properties of the sampled aerosol and can be calculated as a function of the

199   particle single scattering albedo (ω). In this study, because of the absence of an

200   independent determination of ω, we used an estimated "first-guess" single scattering

201   albedo (ω^*) to calculate R. This was determined as the ratio of the measured scattering (σ_s)

202   to extinction (σ_s + σ^*_{abs}) coefficients, with σ^*_{abs} corrected for the scattering and the

203   multiple scattering corrections, but not for the shadowing effect. The obtained $R(\lambda)$

204   varied between 0.75 and 1 for ω^* between 0.75-0.99 at 370 nm and 0.70-0.99 at 950 nm.

205   The whole uncertainty on the absorption coefficient was estimated with the propagation

206   error formula taking into account for the different factors in Eq. (1) and varied between

207   11-36% at 370 nm and 12-70% at 950 nm.

208   It has to be noticed that an enhanced absorption at single wavelengths was observed in

209   several cases for the aethalometer. This was possibly due to the absorption on the exposed

210   filter of gases or volatile compounds absorbing at some of the instrument operating

211   wavelengths (Weingartner et al., 2003). These anomalous points were accurately selected

212   and screened from the dataset. As a result of this screening, data in correspondence of only

213   60% of the considered SLRs were available for aerosols analyses.

214   The measured aerosol scattering and absorption coefficients were used to calculate the

215   particle spectral single scattering albedo between 370 and 950 nm as:

216    $$\omega(\lambda) = \frac{\sigma_s(\lambda)}{\sigma_s(\lambda) + \sigma_{abs}(\lambda)} \qquad (2).$$

217   The uncertainty on ω was calculated with the propagation error formula and varied

218   between 0.02 and 0.04 at all wavelengths.

219   Additionally, for each SLR for which aethalometer data were available, the particle

220   absorption Ångström exponent (AAE) was calculated as the power law fit of the measured

221   absorption coefficients versus wavelength.

222 - The aerosol number size distribution ($dN/dlogD_g$) was measured by two different optical

223   particle spectrometers: the passive cavity aerosol spectrometer probe (PCASP, model 100-

224   X, 1-s resolution, 31 size classes between 0.1 and 3.0 μm diameter, operating wavelength

225   632.8 nm), and the optical particle spectrometer GRIMM (GRIMM Inc., model 1.129, 6-s

226   resolution, 32 size classes between 0.3 and 32 μm diameter, operating wavelength 655

227   nm). For both the PCASP and the GRIMM, the measured sphere-equivalent optical

228   diameter was converted in a sphere-equivalent geometrical diameter (D_g) by taking into

229   account the complex refractive index of the sampled aerosol (Liu and Daum, 2000).

230   Differently from Di Biagio et al. (2015), where the complex refractive index used to

231   correct the size was fixed based on literature values (n=1.52÷1.70, k=0.01 for pollution

232   aerosols in the Mediterranean), here the complex refractive index to correct the size was

233   iteratively adjusted based on optical closure calculations. Full details of the procedure are

234   provided in Sect. 3.2. After optical closure and refractive index correction the D_g range

235   varied between 0.10-4.24 and 0.10-4.84 µm for the PCASP and 0.26-58.75 and 0.30-73.60

236   µm for the GRIMM as a function of the assumed aerosol refractive index. The uncertainty

237   on D_g is between 1 and 25%. For comparison, the D_g values obtained in Di Biagio et al.

238   (2015) were 0.10-4.47 and 0.28-65.80 µm for the PCASP and the GRIMM, respectively.

239   The smallest and the largest size bins of both instruments, for which the minimum and

240   maximum edges respectively are not defined, were excluded from the datasets, thus

241   reducing the PCASP and GRIMM D_g ranges to 0.10-3.94 and 0.11-4.53 µm for the

242   PCASP and 0.28-50.01 and 0.34-63.03 µm for the GRIMM.

243   Corrected data from the PCASP and the GRIMM were then merged to obtain the aerosol

244   size distribution over a larger size range. The two instruments superimpose in a large

245   interval covering the diameter range ~0.30–4.0 µm. In this interval the PCASP and the

246   GRIMM showed a good agreement below 0.4 µm and above 1.0 µm (less than ~10%

247   difference), while significant differences were observed in the 0.4-1.0 µm range where the

248   PCASP underestimates the GRIMM measurements by more than ~50%. This difference is

249   of great relevance in terms of optical properties because particles in the 0.4-1.0 µm size

250   interval are very efficient for interaction with shortwave radiation. With the aim of

251   understanding which of the two instruments measures correctly in the 0.4-1.0 µm range

252   we performed an optical test, which consisted in calculating with Mie theory the scattering

253   coefficient at 450, 550, and 700 nm based on the PCASP and GRIMM size data, and then

254   in comparing it with simultaneous nephelometer measurements. Optical calculations were

255   performed by fixing the complex refractive index at 1.6-0.01i, so at the mean of the range

256   of values reported in the literature for pollution aerosols (Ebert et al., 2002 and 2004;

257   Mallet et al., 2003 and 2011; Müller et al., 2002; Raut and Chazette, 2008). SLRs

258   characterized by a low variability in terms of scattering coefficient and particle

259   concentration were selected. The results of the optical test indicate that in the 0.4-1.0 µm

260   range the size distribution of the GRIMM is more accurate since it permits to most closely

261   reproduce nephelometer observations (<5% mean difference between calculations and

262   observations at the three wavelengths, compared to differences up to 15-21% if PCASP

263   data are used in the 0.4-1.0 μm size range). Thus, a combined PCASP-GRIMM number

264   size distribution $dN/dlogD_g$ in the ~0.10 to 50.01-63.03 μm diameter range was estimated

265   by considering PCASP data up to 0.30 μm and GRIMM data above. The volume size

266   distribution was also computed as $dV/dlogD_g = \pi/6\, D_g^3\, dN/dlogD_g$. Averages of the number

267   and volume size distributions over each SLRs were calculated.

268   Nonetheless, due to a technical problem, GRIMM data were only available below ~350 m

269   (~970 hPa).

270 -   The total particle number concentrations in the ultrafine mode (4 nm-0.1 μm; dN_{UFP}, i.e.

271   formerly defined as Aitken mode in Di Biagio et al., 2015) and accumulation mode (0.1-

272   1.0 μm; dN_{Acc}) were calculated by combining condensation particle counter measurements

273   of particle concentration in the 0.004 − 3 μm range (CPC, TSI Inc., model 3775, 5-s

274   resolution) and size distribution data. Due to the fact that above 350 m the GRIMM was

275   not available, only PCASP data were used in the calculations of dN_{UFP} and dN_{Acc} over the

276   whole altitude range. dN_{UFP} was estimated as the difference between CPC concentration

277   and the integral of PCASP data between 0.1 and 3.0 μm, while dN_{Acc} was obtained by

278   integrating the PCASP number concentrations in the 0.1-1.0 μm interval. The

279   underestimation of the PCASP number concentration between 0.4 and 1.0 μm, as

280   discussed above, was estimated to induce a ~20% underestimation of the dN_{Acc} calculated

281   here, whilst it had almost a negligible impact on dN_{UFP}. The dN_{UFP} and dN_{Acc} obtained in

282   correspondence of each SLR were used to calculate the ultrafine-to-accumulation ratio

283   dN_{UFP}/dN_{Acc}.

284 -   The carbon monoxide (CO) and ozone (O_3) mixing ratios were measured by the MOZART

285   instrument (CO, 30-s resolution and ±5% nominal uncertainty, O_3, 4-s resolution and ±2%

286   nominal uncertainty) (Nedelec et al., 2003). Starting from the measured O_3 and CO, the

287   ozone enhancement ratio ($\Delta O_3/\Delta CO$) was calculated, i.e. the ratio of the ozone to carbon

288   monoxide variations compared to their baseline values. A background value of ~70 ppbv

289   in the boundary layer and ~60 ppbv in the free troposphere was used for CO, while the

290   background was set at ~30 ppbv for O_3 at all levels (Di Biagio et al., 2015). $\Delta O_3/\Delta CO$ data

291   were used together with dN_{UFP}/dN_{Acc} to retrieve information on the age of the sampled air

292   masses, as discussed in Di Biagio et al. (2015).

293   In order to compare SLRs measurements obtained at different altitudes, the data analysed

294   here were reported to standard temperature and pressure (STP) using T=293.15 K and

295   P=1013.25 hPa. In this case, the scattering and absorption coefficients were scaled to STP

296   conditions and the particle concentrations (in number or volume) were given as particles per

297   standard cm^{-3} (scm^{-3}). Where not explicitly indicated, data refer to STP conditions.

298   In Table 2 we summarize main information and uncertainties for the different aerosol

299   instruments considered in this study.

300

301   **3.2 Optical closure and estimation of the aerosol complex refractive index**

302   An optical closure study was realised to estimate the complex refractive index (m=n-ik) of

303   pollution aerosols based on optical and size data. The flowchart of the procedure is illustrated

304   in Fig. 2. Optical closure consisted in recalculating the spectral scattering σ_s and absorption

305   σ_{abs} coefficients measured for each SLR by using the measured size distribution as input and

306   by varying the real (n) and imaginary (k) parts of the complex refractive index in the

307   calculations. Then, n and k were fixed when the best agreement between measurements and

308   calculations was found. Given that the size distribution measured by the PCASP and the

309   GRIMM depends on the aerosol refractive index, the optical-to-geometrical diameter

310   conversion was recalculated at each iteration based on the assumed n and k. Optical

311   calculations were performed using Mie theory for spherical particles. The Mie_single.pro

312   IDL routine available at http://www.atm.ox.ac.uk/code/mie/mie_single.html was used. In the

313   calculations the real part of the refractive index was varied in the range 1.30-1.80 at steps of

314   0.01, while the imaginary part in the range 0.001-0.1 at steps of 0.001, for a total of 5100

315   inversions for each SLR dataset. The uncertainty on the real and imaginary parts of the

316   refractive index was estimated with a sensitivity study. To this purpose, the values of n and k

317   were also obtained by using as input the observed σ_s, σ_{abs}, and $\dfrac{dN}{d \log D_g}$ plus or minus one

318   standard deviation on their measurement. The deviations of the values of n and k retrieved in

319   the sensitivity study with respect to those obtained in the first inversions were assumed to

320   correspond to the one standard deviation uncertainty. The estimated uncertainty was <5% for

321   n and ~25-30% for k.

322

323

324

3.3 Boundary layer height estimation

The planetary boundary layer (BL) top height was estimated from meteorological observations (temperature, T, potential temperature, θ, and relative humidity, RH) for each vertical sounding performed during TRAQA flights (see Di Biagio et al., 2015). The boundary layer top height was between 730 and 1500 m, with an average of ~1000 m. The location of each SLR, so if it is within the boundary layer or in the free troposphere, was determined based on the planetary boundary layer top height estimated from the closest vertical sounding performed during each flight.

3.4 Tracking the origin of the sampled air masses

As discussed in Di Biagio et al. (2015), aerosol observations during TRAQA were mostly influenced by pollution/anthropogenic particles exported from different sources around the basin (Northern Italy/Po Valley, Southern France, Barcelona area). The Lagrangian trajectory model FLEXPART (FLEXible PARTicle dispersion model, Stohl et al., 1998), adapted for the WRF (Weather Research and Forecasting) meteorological input (Brioude et al., 2013) was used here to track the origin of air masses sampled during SLRs. Five-day three-dimensional back-trajectories were calculated using the WRF meteorological output at a 30 km horizontal resolution and 28 vertical model levels up to 50 hPa. The model specific humidity and potential vorticity were also interpolated along the trajectory path. Based on FLEXPART simulations, data for the different SLRs were separated as a function of the origin of the sampled air masses. Three different sectors were defined: the Western sector, which includes trajectories coming from the Atlantic Ocean and travelling over France or northern Spain before reaching the Western basin; the Eastern sector, including air mass trajectories from continental Europe that have travelled over northern Italy-Po Valley before entering the basin; and the Open sea sector, which consists of trajectories coming from the Western or Eastern sectors which have experienced at least 2 days of subsidence over the sea in the Western basin and thus can be taken as representative of the regional background aerosol or local pollution sources, i.e. ship emissions. The three different selected sectors are shown in Fig. 1, while Table 1 also reports the identified sector of origin for the air masses sampled during the different SLRs.

As discussed in Di Biagio et al. (2015), several flights were affected by dust particles exported over the basin from Northern Africa. SLRs data dominated by dust were identified based on the combined analysis of back-trajectories, lidar profiles and optical data, and were

358 excluded from the dataset. However, for some SLRs, the possible mixing of dust aerosols
359 with pollution particles cannot be a priori excluded.

360

361 **3.5 Radiative model calculations**

362 Radiative transfer calculations were performed to estimate the instantaneous aerosol direct
363 radiative effect in the shortwave spectral range for different cases and in clear-sky conditions.
364 The objective of the calculations was to test the sensitivity of the DRE to the variability of the
365 aerosol optical properties, in particular the single scattering albedo, as observed in this study.
366 The GAME radiative transfer model (Dubuisson et al., 1996 and 2006) was used in this study
367 to compute the vertical profiles of downward and upward shortwave irradiances over the
368 0.28-3.0 μm spectral range. The model calculates radiances and irradiances at various
369 atmospheric levels at 400 cm^{-1} spectral resolution between 0.28 and 0.5 μm, and 100 cm^{-1}
370 resolution between 0.5 and 3 μm. Spectral absorption by principal atmospheric gases (H_2O,
371 CO_2, O_3, CH_4, N_2O, O_2) is taken into account in the model. The discrete ordinate method
372 (Stamnes et al., 1988) with twelve streams was used in the simulations to describe multiple
373 scattering. Simulations were performed with and without aerosols by fixing the solar zenith
374 angle (θ) at 60°, i.e. at about the mean of the diurnal value at the latitudes of north-Western
375 Mediterranean, and for a mid-latitude climatological summer meteorological profile. The
376 aerosol optical properties that are used as input in the GAME radiative code are the spectral
377 variation of the optical depth (τ), the asymmetry parameter (g) and the single scattering
378 albedo (ω). The difference of the net shortwave fluxes (downward minus upward irradiances)
379 with and without aerosols at the surface and at TOA was used to estimate the aerosol DRE at
380 these two levels. The atmospheric DRE was then calculated as the difference between the
381 TOA and the surface values. Finally, the ratio of the DRE to the aerosol optical depth at 500
382 nm, i.e. the aerosol forcing efficiency (FE), was obtained. The shortwave heating rate at the
383 altitude z was also calculated as:

384
$$\frac{\partial T}{\partial t} = -\frac{1}{\rho C_p} \frac{\partial F(z)}{\partial z} \quad (3)$$

385 where T is the air temperature, ρ is the air density, C_p is the specific heat of the air, and F(z)
386 is the net flux at the altitude z.

387

388

4. Results

4.1 Overview over the different SLRs

Figure 3 shows the averages altitude, spectral scattering (σ_s) and absorption (σ_{abs}) coefficients, scattering and absorption Ångström exponent (SAE and AAE, respectively), ozone enhancement factor ($\Delta O_3/\Delta CO$), and ultrafine-to-accumulation particle ratio (dN_{UFP}/dN_{Acc}) measured for the different SLRs during TRAQA.

As shown in Fig. 3 and Table 1, the large majority of the SLRs were performed within the boundary layer at an altitude <1000 m. Only four SLRs (V25_R2, V25_R3, V26_R1, and V30_R1) measured aerosols in the free troposphere between 1800 and 3500 m. The sampled aerosols originated in each of the three different source sectors identified based on FLEXPART back-trajectories (Western, Eastern, and Open sea), with a larger number of cases from the Western sector compared to the Eastern and the Open sea areas.

For all the different cases, the measured scattering coefficient was in the range 16-73 Mm^{-1} at 450 nm and 8-30 Mm^{-1} at 700 nm. The absorption coefficient was generally below 10 Mm^{-1} at all wavelengths, with the exception of V27_R1 and V32_R1 for which values up to ~20 Mm^{-1} at 370 nm were measured. For these two cases also the highest values of the particle concentration in the accumulation mode (~1700-2200 # cm^{-3}, not shown) and among the highest values of the scattering coefficient were measured. For all cases, both σ_s and σ_{abs} decrease with the wavelength. The pronounced spectral variability of σ_s, in particular, indicates the dominance of pollution/anthropogenic fine particles in the sampled plumes.

The SAE varied between 0.96 and 1.94, while the AAE varied between 0.92 and 1.65, with an average of ~1.20. The AAE was not calculated for few cases with very low values of the absorption coefficient (σ_{abs} at 370 nm < 1.5 Mm^{-1}). Both the SAE and the AAE obtained in this study fall in the range of variability indicated by several authors to identify pollution/anthropogenic aerosols or pollution mixed with other aerosol types in the Mediterranean basin (SAE>1-1.5, and AAE~1-1.5; Pace et al., 2006; Toledano et al., 2007; Mallet et al., 2013). Values of AAE larger than unity, in particular, might suggest the possible mixing of pollution with brown carbon or dust particles over the basin (Russell et al., 2010; Mallet et al., 2013).

For all the measured SLRs the $\Delta O_3/\Delta CO$ and the dN_{UFP}/dN_{Acc} ratios varied in the range 0.37-1.02 and 1-50, respectively, for O_3 and CO varying between 24-78 and 69-136 ppbv and dN_{UFP} and dN_{Acc} between 320-22500 and 100-2170 # cm^{-3}. $\Delta O_3/\Delta CO$ and the dN_{UFP}/dN_{Acc} are linked to the photochemical (rate of ozone formation) and physical (rate of ultrafine to

422 accumulation particle conversion) processes responsible for the aging of the aerosol plumes.

423 The range of measured values here includes both cases with high dN_{UFP}/dN_{Acc} and low

424 $\Delta O_3/\Delta CO$, typical of fresh plumes, and cases with low dN_{UFP}/dN_{Acc} and high $\Delta O_3/\Delta CO$,

425 indicative of more aged air masses (Di Biagio et al., 2015).

426 The summary of observations from Fig. 3 suggests that the set of SLRs measurements

427 considered in this study can be considered representative of a wide range of different

428 atmospheric conditions occurring over the basin both in terms of sources, loadings, and

429 lifetime for pollution aerosols.

430

431 **4.2 Particle size distributions**

432 Figure 4 shows the mean and the range of variability of the number and volume size

433 distributions measured during horizontal SLRs within pollution layers during TRAQA. Data

434 were separated based on the origin of the sampled air masses and refer only to cases at <350

435 m altitude within the boundary layer. The absolute uncertainty on the measured

436 concentration, as also reported in Table 2, is ~15% for particle diameters below 0.31 µm and

437 ~10% at larger sizes. The grey shading indicates considerable variability in the number

438 concentration of the size distributions, of approximately one order of magnitude for much of

439 the size range measured. This reflects the relative wide range of aerosol loadings encountered

440 during the campaign. The minimum of the size distribution over the whole diameter range

441 was measured in the Western sector (V32_R3), whilst the largest number concentrations in

442 the super-micron range were observed in correspondence of V19_R1 and V32_R1. For all the

443 other SLRs, the size distributions were very similar, especially at diameters below ~5 µm.

444 The measured number size distribution from each SLR was fitted with multi-mode lognormal

445 functions:

446
$$\frac{dN}{d\log D_g} = \sum_i \frac{N_{tot,i}}{\sqrt{2\pi}\log\sigma_{g,i}} \left(-\frac{\left(\log D_p - \log D_{g,i}\right)^2}{2\log^2\sigma_{g,i}} \right) \qquad (4).$$

447 For each mode i, N_{tot} represents the total aerosol number concentration, D_g the median

448 diameter, and σ_g the geometric standard deviation. The logarithm refers to base 10. Size data

449 were fitted automatically using the MPCURVEFIT IDL routine available at

450 http://www.physics.wisc.edu/~craigm/idl/fitting.html. Since the aim of the fitting is to

451 describe as closely as possible the measured number size distributions for subsequent optical

452 calculations (Sect. 4.4), up to seven modes were used to fit the data. The correlation

453 coefficient for the fit functions was larger than 0.97 for all cases. The parameters of the

454 lognormal fits are reported in Table 3. The first mode of the size distribution is generally at

455 0.13-0.14 µm, whilst the largest mode is between ~5 and 8 µm for the different cases.

456

4.3 Spectral single scattering albedo: variability as a function of air mass origin and

458 **height**

459 Figure 5 shows the spectral ω for the different SLRs considered in this study. Data were

460 separated based on the origin of the sampled air masses. The single scattering albedo varies in

461 the range 0.84-0.98 at 370 nm and 0.70-0.99 at 950 nm and generally decreases with the

462 wavelength, as it is typical for pollution particles (Dubovik et al., 2002). Only in two cases

463 (V19_R1 and V30_R2) the single scattering albedo increases with wavelength. For these

464 cases also very high values of ω were observed (0.92-0.97 for V19_R1 and 0.98-1.0 for

465 V30_R2), which may suggest the possible mixing of pollution with sea spray or desert dust

466 particles, both showing low absorption in the shortwave range (Bergstrom et al., 2007). The

467 lowest values of the single scattering albedo were measured for V27_R1 (0.84-0.70 between

468 370 and 950 nm) sampled at ~160 m and originated in the Open Sea sector. Data in Fig. 3

469 also indicate for V27_R1 very low values of $\Delta O_3/\Delta CO$ (~0.37) and a relatively high

470 dN_{UFP}/dN_{Acc} (~7), which suggests that V27_R1 was a fresh plume possibly associated to

471 local emissions, i.e. ship plumes, over the basin. If we exclude V27_R1, the range of

472 measured values appears comparable (within error bars) for the three considered sectors

473 (Western, Eastern, and Open sea; ω between 0.88 and 0.98 at 370 nm and 0.83 and 0.99 at

474 950 nm).

475 The vertical variability of ω, together with dN_{UFP}/dN_{Acc}, $\Delta O_3/\Delta CO$, SAE, and AAE, is shown

476 in Fig. 6 for the different considered cases. With the only exception of V27_R1, for which the

477 lowest values were observed below 200 m, the single scattering albedo does not show a clear

478 trend with height, with a similar range of values measured in the boundary layer, below

479 ~1000 m, and in the free troposphere up to ~3500 m. As for ω, the AAE does not

480 significantly vary with height. At the same time, dN_{UFP}/dN_{Acc} and SAE decrease with height,

481 with a concurrent slight $\Delta O_3/\Delta CO$ increase, which may suggest an increase of plume age

482 with height. The ensemble of these observations seems to indicate that, for our observed

483 cases, the absorptivity properties of the sampled plumes do not depend on the altitude and

484 associated air mass age of the plume. It should be pointed out, however, that the majority of

485   cases considered here were sampled below 1000 m, so in the boundary layer, and the

486   statistics in the free troposphere is only limited to a few events.

487   Values of the single scattering albedo measured in this study are comparable with values

488   reported at several other sites in the Central and Western Mediterranean region for pollution

489   aerosols (Mallet et al., 2003 and 2013; Meloni et al., 2006; Saha et al., 2008; Di Biagio et al.,

490   2009; Pandolfi et al., 2011). The single scattering albedo from these studies varies in the

491   range 0.84-0.95 at 440 nm, 0.76-0.98 at 500-550 nm, and 0.80-0.87 at 870 nm. Compared

492   with the literature, larger and lower values are obtained in the present study for few cases

493   mostly influenced by sea spray, desert dust, and local fresh emissions, respectively.

494

495   **4.4 Complex refractive index of pollution aerosols**

496   As discussed in the previous section, the single scattering albedo of pollution aerosols shows

497   a relatively large variability. Here we investigate the impact of this variability on the complex

498   refractive index ($m=n-ik$) of the particles.

499   For eight selected SLRs for which both complete optical (scattering and absorption

500   coefficients, and single scattering albedo) and size distribution measurements were available,

501   the aerosol spectral complex refractive index was estimated by optical closure study as

502   described in Sect. 3.2. These cases correspond to V19_R1, V21_R1, V21_R3, V23_R2,

503   V27_R1, V31_R1, V32_R1, V32_R3 sampled within the boundary layer at <350 m altitude.

504   The comparison of the measured and modelled σ_s and σ_{abs} are shown in Fig. 7, while the

505   retrieved real and imaginary parts of the refractive index for the different SLRs are reported

506   in Fig. 8. Data in Fig. 8 are also compared to the real and imaginary parts of the refractive

507   index for the single components (insoluble, water soluble, soot, and sea salt) considered in

508   the OPAC model (Optical Properties of Aerosols and Clouds, Hess et al., 1998) to represent

509   continental, urban and maritime polluted aerosols. As shown in Fig. 7, a very good agreement

510   was found between the calculated and the measured scattering and absorption coefficients,

511   with an average difference of less than 5% for both σ_s and σ_{abs}. For our analysed cases n and

512   k vary in the range 1.67-1.75 and 0.004-0.050 at 370 nm and 1.41-1.77 and 0.002-0.097 at

513   950 nm, respectively. The imaginary part of the refractive index slightly increases with

514   wavelength, while not a clear tendency is found for the real part, which in some of the cases

515   increases with wavelength and in others decreases. Highest values of k are obtained for

516   V27_R1, which also shows the absolute lowest values of ω in our dataset (0.84-0.70),

517   followed by V32_R1 and V32_R3, which also present relatively low values of ω (0.92-0.83).

518 The lowest k, as well as among the lowest n, is instead obtained for V19_R1 (ω=0.92-0.96).

519 The comparison of our data with OPAC values for single components suggests that in most

520 cases particles are composed of a mixing of insoluble and water soluble components, with

521 possible contributions of soot (V27_R1) ad sea salt (V19_R1).

522 The results of the complex refractive index obtained in this study are in agreement with

523 previous estimates obtained for pollution aerosols in continental Europe (n~1.50-1.72 and

524 k~0.001-0.1 for UV-visible wavelengths e.g. Ebert et al., 2002, 2004; Müller et al., 2002;

525 Mallet et al., 2003, 2011; Raut and Chazette, 2008). Larger values of both n and k are instead

526 obtained here compared to AERONET retrievals at different sites in the Western

527 Mediterranean (1.38-1.46 for n and 0.003-0.01 for k at 440 and 670 nm; Mallet et al., 2013).

528 Figure 9 shows the results of the correlation analysis between the single scattering albedo and

529 the complex refractive index obtained for the analysed cases. For the real part, the range of

530 retrieved n values is larger (1.41-1.74) for ω greater than ~0.95, while as the single scattering

531 albedo decreases the real part converges to ~1.65-1.75 at all wavelengths. A strong

532 correlation is observed between ω and k at all wavelengths, that is the lower the single

533 scattering albedo, the higher the imaginary part. A linear regression fit was applied to the ω-k

534 datasets at the seven wavelengths. The slope of the fit varies between -2.2 and -6.9, and

535 decreases with the wavelength (in particular if the outlier points of k in correspondence of

536 V27_R1 are eliminated), in agreement with the decrease of ω with λ for pollution aerosols.

537 The intercept for all cases is lower than 1 (0.93-0.97), with lowest values obtained at 880 and

538 950 nm. This is possibly associated to a slight underestimation of ω which, especially at these

539 wavelengths, is difficult to determine given the high uncertainty on the particle absorption

540 coefficient. Another source of uncertainty is the size distribution, which influences the results

541 of Mie calculations, and thus has a direct impact on the refractive index retrieval.

542

4.5 Influence of the single scattering albedo variability on the aerosol direct shortwave
543

544 **radiative effect (DRE)**

545 Radiative transfer model calculations with the GAME model were performed with the aim of

546 investigating the impact of the variable optical properties, and in particular the single

547 scattering albedo, on the shortwave direct radiative effect of pollution particles in the Western

548 Mediterranean basin.

549 Simulations were performed by considering three different vertical aerosol profiles, based on

550 observations reported by Di Biagio et al. (2015): i. aerosols only confined in the BL (whose

551   altitude is fixed at 1000 m, in the mean of observations during TRAQA); ii. 50% of the

552   aerosol optical depth in the BL and 50% in the FT (which is considered to extend between

553   1000 and 4000 m); iii. 20% of the aerosol optical depth in the BL and 80% in the FT. For the

554   different cases we fixed the total aerosol optical depth at 0.2 at 550 nm, which corresponds to

555   the mean of observations obtained over the Western basin during TRAQA (Di Biagio et al.,

556   2015). However, results will be given as FE, so they are independent on the chosen optical

557   depth. We assumed a uniform aerosol distribution and constant optical properties within the

558   BL and the FT for the three different considered profiles. This assumption comes from the

559   observations of the present study, which do not evidence any significant change of the

560   aerosol properties with height. Aerosol spectral optical properties, both in the BL and in the

561   FT up to 4000 m, were assumed from observations, as explained in the following.

562   The GAME model requires as input the aerosol optical depth, single scattering albedo, and

563   asymmetry factor at 7 wavelengths between 330 and 1500 nm. The spectral optical depth

564   between 330 and 1500 nm was extrapolated from the fixed value of 0.2 at 550 nm by

565   assuming a Ångström exponent of 1.5, in the mean of our observations for pollution aerosols

566   (see Fig. 2). For the single scattering albedo, we considered 3 different sets of values which

567   correspond to the minimum, maximum, and mean of the values observed in this study (the

568   absolute minimum for V27_R1 was excluded for calculations since it represents an outlier in

569   our data). The ω values at 370-950 nm as obtained from experimental data were then

570   extrapolated at the 7 GAME wavelengths (Table 4). The asymmetry factor was calculated

571   from Mie theory based on the refractive index values and size distribution data for the eight

572   cases considered in the previous Section. The spectral variation of g used in the radiative

573   transfer calculations was estimated as the mean of the values obtained for these eight cases

574   extrapolated at the 7 GAME wavelengths. The obtained g varied between 0.60 at 330 nm and

575   0.51 at 1500 nm. These values are consistent with previous estimates of g obtained for

576   pollution aerosols over the Mediterranean basin (Meloni et al., 2006; Saha et al., 2008; Mallet

577   et al., 2011).

578   Background stratospheric aerosols (above 12 km) were also taken into account for radiative

579   calculations; optical properties from the OPAC stratospheric aerosol model (Hess et al.,

580   1998) were assumed.

581   Finally, in addition to aerosol optical properties, the GAME model requires as input the

582   albedo of the surface (A_S) at 5 wavelengths between 448 nm and 2130 nm. In this study,

583   simulations were performed over the sea surface. The albedo of the sea surface was obtained

584 from Jin et al. (2004), which provide a parameterisation of A_S as a function of chlorophyll
585 concentration (Chl), wind speed (w), aerosol optical depth at 500 nm (τ), and the solar zenith
586 angle (θ). For this study A_S was estimated for Chl=0, w=6-9 m s^{-1}, τ=0.24 (extrapolated from
587 the value of 0.2 at 550 nm), and θ=60°, and it varied between 0.009 and 0.005 in the
588 considered 448-2130 nm spectral range.

589 Results of the radiative transfer simulations are shown in Fig. 10, which reports the FE at the
590 surface, TOA, and atmosphere (FE_S, FE_{TOA} and FE_{ATM}) for the maximum, mean, and
591 minimum of the single scattering albedo observed in this study. Results of the simulations are
592 mostly independent on the vertical distribution of the aerosols (less than ~5% changes for
593 FE_S, FE_{ATM}, and FE_{TOA} for the three different profiles used in the simulations), so the mean
594 of the results obtained for the three cases is reported in Fig. 10. The forcing efficiency varies
595 between -160 and -235 (FE_S), -137 and -92 (FE_{TOA}), and +23 and +143 (FE_{ATM}) W m^{-2} τ^{-1} for
596 ω varying between its maximum and minimum values. Estimates of the forcing efficiencies
597 in correspondence of the mean of ω are -198, -113, and +85 W m^{-2} τ^{-1} at the surface, TOA,
598 and atmosphere, respectively. The corresponding instantaneous shortwave heating rate at the
599 surface varies between 0.2 and 2.0 K day^{-1} for ω between its maximum and minimum.

600 As expected, the lower the single scattering albedo, the larger in absolute value the FE_S and
601 FE_{ATM} and the lower the FE_{TOA}. This is due to the impact of absorption on the amount of
602 radiation trapped in the atmosphere and transmitted towards the surface, which thus enhance
603 the radiative effect in the atmosphere and at the surface for decreasing ω. Conversely, the
604 larger the particle absorption, the lower the effect on the radiation reflected back to space,
605 and thus the decrease of the intensity of the cooling effect at the TOA. Changes in the single
606 scattering albedo of the particles between its maximum and minimum ($\Delta\omega$=0.1-0.2 at the
607 different wavelengths) determine about a 50% strengthening of the direct shortwave radiative
608 effect at the surface, and a reduction of ~30% the effect at the TOA. Consequently, the
609 atmospheric FE may vary up to an order of magnitude. These results thus highlight the
610 sensitivity of the DRE on the absorptivity properties of the particles, as well as the
611 importance of accurately reproducing the single scattering albedo of aerosols to correctly
612 evaluate their direct radiative effect.

613 The results of the present study are in quite good agreement with previous estimates of the
614 aerosol forcing efficiency for pollution aerosols in the Mediterranean area. FE_S, FE_{ATM}, and
615 FE_{TOA} obtained here compare well with data obtained in the Central Mediterranean by Di
616 Biagio et al. (2009, 2010), who provide estimates based only on observational data, i.e.
617 without any assumption on the aerosol optical properties. In these studies they report a

618 forcing efficiency of ~-200 and -164 W m^{-2} τ^{-1} at the surface and TOA at solar zenith angles

619 of 50°-60° for mixed aerosols (pollution plus sea salt particles). They estimate an increase in

620 absolute value of FE$_S$ of about 20-40% due to a decrease of 0.1-0.2 of the single scattering

621 albedo (at 415 and 868 nm) of the aerosols, as well as a concurrent increase of FE$_{TOA}$ of

622 about 10-40%. The observations obtained in this study fall in the range of variability reported

623 by Di Biagio et al. (2009, 2010). Our data also agree with estimates of Saha et al. (2008),

624 reporting for pollution aerosols measured in the French Mediterranean coast up to 40%

625 variability in the FE$_S$ and FE$_{TOA}$, concurrently with 70% increase of FE$_{ATM}$, due to a ω

626 change of 0.15 at 525 nm. Conversely, our estimates at the surface and TOA are larger in

627 absolute value compared to data reported for continental Europe by Horvath et al. (2002),

628 who estimated a FE$_S$ of ~-164 W m^{-2} τ^{-1} and a FE$_{TOA}$ of -50 W m^{-2} τ^{-1} for polluted aerosols

629 with ω=0.90 at 520 nm, thus comparable with our mean values of single scattering albedo for

630 pollution aerosols.

631

632 **5. Conclusions**

633 In this study we have presented measurements of the spectral optical properties (scattering

634 and absorption coefficients and single scattering albedo) and particle size distributions for

635 pollution aerosols obtained over the remote sea in the Western Mediterranean basin during

636 the TRAQA campaign in summer 2012. The set of observations analysed in this study can be

637 assumed to be representatives of a wide range of different conditions that can be observed

638 over the basin, both in terms of pollution sources, aerosol loadings, and lifetimes of the

639 plumes. The detailed characterization of the spectral optical properties of pollution aerosols

640 in the Western basin was missing to date.

641 Observations from the present study show a large variability of the optical properties of

642 pollution aerosols over the basin, in particular of the spectral single scattering albedo. Values

643 of ω in the range 0.84-0.98 at 370 nm and 0.70-0.99 at 950 nm are observed in this study.

644 This variability of ω does not seem to be clearly linked neither to the particle origin, nor to

645 the altitude and associated aging of the sampled plumes. The variability of ω reflects in a

646 large variability for the complex refractive index of pollution aerosols, which is estimated to

647 span in the range 1.41-1.75 for the real part and 0.002-0.068 for the imaginary part between

648 370 and 950 nm. The analysis of the complex refractive index suggests that possible

649 differences in terms of particle compositions can explain in part the observed variability of ω.

650 A large range of compositions has been however reported for pollution aerosols in Europe

651   and the Mediterranean basin (Mallet et al., 2003; Ebert et al., 2004; Pey et al., 2010; Piazzola

652   et al., 2012) and a more detailed analysis of the aerosol composition for the cases measured

653   here should be addressed.

654   Based on the observations of the present study, the variability of optical properties for

655   pollution aerosols can arise from the combination of different factors, linked to the origin,

656   production mechanism, and aging of the plumes along their lifetime, as well as the possible

657   mixing of different plumes with different characteristics. So, the inherent heterogeneity of

658   sources, coexistence of different air masses, and multiple physical and chemical processes

659   occurring in a complex environment such as the Western Mediterranean may give rise to this

660   inherent variability of the particle single scattering albedo.

661   This observed variability on ω has a large influence on the direct shortwave radiative effect

662   of pollution aerosols at the surface, TOA, and within the atmosphere. For instance, a change

663   of up to an order of magnitude (from +23 to +143 W m^{-2} τ^{-1} at 60° solar zenith angle) in the

664   atmospheric radiative effect is estimated due to the variability of the single scattering albedo

665   within the range of values observed in this study. The change in the amount of atmospheric

666   absorbed solar radiation may have a strong impact on the temperature profile and the

667   atmospheric thermal structure, with important consequences on several processes, such as

668   cloud formation and precipitations. The strong sensitivity of the DRE also at the surface, up

669   to 50% for varying ω, on its turn, may largely impact the rate of evaporation over the basin,

670   which is also a crucial component of the hydrological cycle (Nabat et al., 2015). Given the

671   large sensitivity of the Mediterranean area and the high risk of desertification for this region

672   (Giorgi and Lionello, 2008; IPCC, 2013) any factor possibly impacting the hydrological cycle

673   should be taken carefully into account by regional climate models. In this view, results from

674   the present study can be used to provide a constraint of the absorption properties of pollution

675   particles in the Western Mediterranean basin to use in regional modelling studies.

676   Constraining these properties constitutes a crucial step in order to better assess the role of

677   aerosols on the radiative balance of this region and to ameliorate the capability of making

678   projection on future climate changes.

679

Author contributions

681   J.-L. Attié, F. Ravetta, G. Ancellet, and P. Formenti designed the TRAQA experiment and

682   coordinated the campaign. C. Gaimoz, N. Grand, and C. Di Biagio operated the instruments

683   on board the ATR-42 during the flights. C. Di Biagio performed the data analysis with

684 contributions from L. Doppler and P. Formenti. S. Bucci and F. Fierli performed the
685 FLEXPART simulations. M. Mallet and P. Dubuisson provided the GAME code for radiative
686 calculations. C. Di Biagio wrote the manuscript with contributions from all co-authors.

687

Acknowledgements

689 All measurement presented here are from the Chemistry-Aerosol Mediterranean Experiment
690 project (ChArMEx, http://charmex.lsce.ipsl.fr), which is the atmospheric component of the
691 French multidisplinary program MISTRALS (Mediterranean Integrated Studies aT Regional
692 And Local Scales). ChArMEx-France was principally funded by INSU, ADEME, ANR,
693 CNES, CTC (Corsica region), EU/FEDER, Météo-France, and CEA. TRAQA was funded by
694 ADEME/PRIMEQUAL and MISTRALS/ChArMEx programmes and Observatoire Midi-
695 Pyrénées. C. Di Biagio thanks the Centre National des Etudes Spatiales (CNES) for financial
696 support.
697 The authors wish to thank the technicians, pilots and ground crew of SAFIRE (Service des
698 Avions Francais Instruments pour la Recherche en Environnement) for facilitating the
699 instrument integration and conducting flying operations. We thank S. Chevaillier, R. Loisil, J.
700 Pelon, and P. Zapf for their contribution during the campaign. We also wish to thank G. Siour
701 for his help to run the GAME radiative code. Helpful comments and suggestions by two
702 anonymous reviewers are acknowledged.

703

References

705 Anderson, T. L. and Ogren, J. A.: Determining aerosol radiative properties using the TSI 3563
706   integrating nephelometer, Aerosol Sci. Technol., 29, 57–69, 1998.

707 Arnott, W., Hamasha, K., Moosmüller, H., Sheridan, P. J. , and Ogren, J. A.: Towards aerosol light-
708   absorption measurements with a 7-wavelength aethalometer: Evaluation with a photoacoustic
709   instrument and 3-wavelength nephelometer, Aerosol Sci. Tech., 39(1), 17–29, 2005.

710 Bergstrom, R. W., Pilewskie, P., Russell, P. B., Redemann, J., Bond, T. C., Quinn, P. K., and Sierau,
711   B.: Spectral absorption properties of atmospheric aerosols, Atmos. Chem. Phys., 7, 5937-5943,
712   2007.

713 Boucher, O., et al., Clouds and Aerosols. Stocker, T., & Qin, D. (eds), Climate Change 2013: The
714   Physical Science Basis. Contribution of Working Group I to the Fifth Assessment Report of the
715   Intergovernmental Panel on Climate Change. Cambridge Univ. Press, Cambridge, United
716   Kingdom and New York, NY, USA, 2013.

717 Brioude, J., Arnold, D., Stohl, A., Cassiani, M., Morton, D., Seibert, P., Angevine, W., Evan, S.,
718   Dingwell, A., Fast, J. D., Easter, R. C., Pisso, I., Burkhart, J., and Wotawa, G.: The Lagrangian
719   particle dispersion model FLEXPART-WRF version 3.1, Geosci. Model Dev., 6, 1889-1904,
720   doi:10.5194/gmd-6-1889-2013, 2013.

721 Collaud Coen, M., Weingartner, E., Apituley, A., Ceburnis, D., Fierz-Schmidhauser, R., Flentje, H.,
722   Henzing, J. S., Jennings, S. G., Moerman, M., Petzold, A., Schmid, O., and Baltensperger, U.:
723   Minimizing light absorption measurement artifacts of the Aethalometer: evaluation of five
724   correction algorithms, Atmos. Meas. Tech., 3, 457–474, doi:10.5194/amt-3-457-2010, 2010.

725 Di Biagio, C., di Sarra, A., Meloni, D., Monteleone, F., Piacentino, S., and Sferlazzo, D.:
726   Measurements of Mediterranean aerosol radiative forcing and influence of the single scattering
727   albedo, J. Geophys. Res., 114, D06211, doi:10.1029/2008JD011037, 2009.

728 Di Biagio, C., di Sarra, A., and D. Meloni, D.: Large atmospheric shortwave radiative forcing by
729   Mediterranean aerosol derived from simultaneous ground-based and spaceborne observations, and
730   dependence on the aerosol type and single scattering albedo, J. Geophys. Res., 115, D10209, doi:
731   10.1029/2009JD012697, 2010.

732 Di Biagio, C., Doppler, L., Gaimoz, C., Grand, N., Ancellet, G., Raut, J.-C., Beekmann, M.,
733   Borbon, A., Sartelet, K., Attié, J.-L., Ravetta, F., and Formenti, P.: Continental pollution in the
734   western Mediterranean basin: vertical profiles of aerosol and trace gases measured over the sea
735   during TRAQA 2012 and SAFMED 2013, Atmos. Chem. Phys., 15, 9611-9630, doi:10.5194/acp-
736   15-9611-2015, 2015.

737 Dubovik, O., Holben, B., Eck, T. F., Smirnov, A., Kaufman, Y. J., King, M. D., Tanré, D., and
738   Slutsker, I.: Variability of absorption and optical properties of key aerosol types observed in
739   worldwide locations, J. Atmos. Sci., 59, 590–608, 2002.

740 Dubuisson, P., Buriez, J. C. and Fouquart, Y.: High spectral resolution solar radiative transfer in
741   absorbing and scattering media: Application to the satellite simulation, J. Quant. Spectrosc. Radiat.
742   Transfer, 55, 103–126, 1996.

743 Dubuisson, P., Roger, J., Mallet, M., and Dubovik, O.: A Code to Compute the Direct Solar Radiative
744   Forcing: Application to An- thropogenic Aerosols during the Escompte Experiment, Proc. In-
745   ternational Radiation Symposium (IRS 2004) on Current Prob- lems in Atmospheric Radiation,
746   edited by: Fischer, H., Sohn, B.- J., and Deepak, A., Hampton, 127–130, 23–28 August 2004, Bu-
747   san, Korea, 2006.

748 Ebert, M., Weinbruch, S., Rausch, A., Gorzawski, G., Hoffmann, P., Wex, H., and Helas, G.: The
749   complex refractive index of aerosols during LACE 98 as derived from the analysis of individual
750   particles, J. Geophys. Res., 107, D21, 8121, doi:10.1029/2000JD000195, 2002.

751 Ebert, M., Weinbruch, S., Hoffmann, P., and Ortner, H. M.: The chemical composition and complex
752   refractive index of rural and urban influenced aerosols determined by individual particle analysis,
753   Atmos. Environ., 38, 6531–6545, 2004.

754 Estellés, V., Martínez-Lozano, J. A., Utrillas, M. P., and Campanelli, M.: Columnar aerosol properties
755   in Valencia (Spain) by ground-based Sun photometry, J. Geophys. Res., 112, D11201,
756   doi:10.1029/2006JD008167, 2007.

757 Esteve, A. R., Ogren, J. A., Sheridan, P. J., Andrews, E., Holben, B. N., and Utrillas, M. P.: Sources
758   of discrepancy between aerosol optical depth obtained from AERONET and in-situ aircraft
759   profiles, Atmos. Chem. Phys., 12, 2987-3003, doi:10.5194/acp-12-2987-2012, 2012.

760 Giorgi, F., and Lionello, P.: Climate change projections for the Mediterranean region. Global Planet
761   Change, 63, 90-104. doi:10.1016/j.gloplacha.2007.09.005, 2008.

762 Gkikas, A., Houssos, E. E., Hatzianastassiou, N., Papadimas C. D., and Bartzokas, A.: Synoptic
763   conditions favouring the occurrence of aerosol episodes over the broader Mediterranean basin Q. J.
764   R. Meteorol. Soc. 138: 932–949, 2012.

765 Hess, M., Koepke, P., and Schult, I.: Optical properties of aerosols and clouds: The software package
766   OPAC, Bull. Am. Meteorol. Soc, 79, 831–844, 1998.

Horvath, H., Alados Arboledas, L., Olmo, F. J., Jovanovic, O., Gangl, M., Sanchez, C., Sauerzopf, H., and Seidl, S.: Optical characteristics of the aerosol in Spain and Austria and its effect on radiative forcing, J. Geophys. Res., 107, 4386, doi: 10.1029/2001JD001472, 2002.

IPCC, 2013: Climate Change 2013: The Physical Science Basis. Contribution of Working Group I to the Fifth Assessment Report of the Intergovernmental Panel on Climate Change [Stocker, T.F., D. Qin, G.-K. Plattner, M. Tignor, S.K. Allen, J. Boschung, A. Nauels, Y. Xia, V. Bex and P.M. Midgley (eds.)]. Cambridge University Press, Cambridge, United Kingdom and New York, NY, USA, 1535 pp, doi:10.1017/CBO9781107415324.

Jin, Z., Charlock, T. P., Smith Jr., W. L., and Rutledge, K.: A parametrization of ocean surface albedo, Geophys. Res. Lett., 31, L22301, doi:10.1029/2004GL021180, 2004.

Lelieveld, J., Berresheim, H., Borrmann, S., et al.: Global air pollution crossroads over the Mediterranean, Science, 298, 794–799, 2002.

Liu, Y. and Daum, P.: The effect of refractive index on size distributions and light scattering coefficients derived from optical particle counters, J. Aerosol Sci., 31, 945–957, 2000.Loeb, N. G., and Su, W.: Direct Aerosol Radiative Forcing Uncertainty Based on a Radiative Perturbation Analysis, J. Climate, 23, 5288–5293. doi: http://dx.doi.org/10.1175/2010JCLI3543.1, 2010.

Loeb, N. G., and Su, W. Y.: Direct aerosol radiative forcing uncertainty based on a radiative perturbation analysis, J. Clim., 23, 5288–5293, 2010.

Lyamani, , H., Olmo, F. J., Alcántara, A., and Alados-Arboledas, L.: Atmospheric aerosols during the 2003 heat wave in southeastern Spain. I: Spectral optical depth, Atmos. Environ., *40*, 6453–6464, 2006.

Lyamani, H., Valenzuela, A., Perez-Ramirez, D., Toledano, C., Granados-Muñoz, M. J., Olmo, F. J., and Alados-Arboledas, L.: Aerosol properties over the western Mediterranean basin: temporal and spatial variability, Atmos. Chem. Phys., 15, 2473-2486, doi:10.5194/acp-15-2473-2015, 2015

Mallet, M., Roger, J. C., Despiau, S., Dubovik, O., and Putaud, J. P.: Microphysical and optical properties of aerosol particles in urban zone during ESCOMPTE, Atmos. Res., 69, 73–97, 15 2003.

Mallet, M., Van Dingenen, R., Roger, J. C., Despiau, S., and Cachier, H.: In situ airborne measurements of aerosol optical properties during photochemical pollution events, J. Geophys. Res., 110, D03205, doi:10.1029/2004JD005139, 2005.

Mallet, M., Gomes, L., Solmon, F., Sellegri, K., Pont, V., Roger, J. C., Missamou, T., and Piazzola, J.: Calculation of key optical properties of the main anthropogenic aerosols over the Western French coastal Mediterranean Sea, Atmos. Res., 101, 396–411, 2011.

Mallet, M., Dubovik, O., Nabat, P., Dulac, F., Kahn, R., Sciare, J., Paronis, D., and Léon, J. F.: Absorption properties of Mediterranean aerosols obtained from multi-year ground-based remote sensing observations, Atmos. Chem. Phys., 13, 9195-9210, doi:10.5194/acp-13-9195-2013, 2013.

McComiskey, A., Schwartz, S. E., Schmid, B., Guan, H., Lewis, E. R., Ricchiazzi, P., and Ogren, J. A.: Direct aerosol forcing: Calculation from observables and sensitivities to inputs, J. Geophys. Res., 113, D09202, doi:10.1029/2007JD009170, 2008.

Meloni, D., di Sarra, A., Pace, G., and Monteleone, F.: Aerosol optical properties at Lampedusa (Central Mediterranean). 2. Determination of single scattering albedo at two wavelengths for different aerosol types, Atmos. Chem. Phys., 6, 715-727, doi:10.5194/acp-6-715-2006, 2006.

Millán, M. M., Mantilla, E., Salvador, R., Carratala, A., Sanz, M. J., Alonso, L., Gangoiti, G., and Navazo, M.: Ozone cycles in the western Mediterranean basin: interpretation of monitoring data in complex terrain, J. Appl. Meteorol., 4, 487–507, 2000.

Müller, D., Ansmann, A., Wagner, F., Franke, K., and Althausen, D.: European pollution outbreaks during ACE 2: Microphysical particle properties and single-scattering albedo inferred from

814 multiwavelength lidar observations, J. Geophys. Res., 107, D15, 4248, 10.1029/2001JD001110,
815 2002.

816 Nabat, P., Somot, S., Mallet, M., Sevault, F., Chiacchio, M. and Wild, M.: Direct and semi-direct
817 aerosol radiative effect on the Mediterranean climate variability using a coupled Regional Climate
818 System Model Clim. Dyn., 44, 1127-1155, doi:10.1007/s00382-014-2205-6, 2015.

819 Nedélec, P., Cammas, J.-P., Thouret, V., Athier, G., Cousin, J.-M., Legrand, C., Abonnel, C.,
820 Lecoeur, F., Cayez, G., and Marizy, C.: An improved infrared carbon monoxide analyser for
821 routine measurements aboard commercial Airbus aircraft: technical validation and first scientific
822 results of the MOZAIC III programme, Atmos. Chem. Phys., 3, 1551–1564, doi:10.5194/acp-3-
823 1551-2003, 2003.

824 Pace, G., di Sarra, A., Meloni, D., Piacentino, S., Chamard, P.: Aerosol optical properties at
825 Lampedusa (Central Mediterranean). 1. Influence of transport and identification of different
826 aerosol types, Atmos. Chem. Phys., 6, 697–713, 2006.

827 Pandolfi, M., Cusack, M., Alastuey, A., and Querol, X.: Variability of aerosol optical properties in the
828 Western Mediterranean Basin Atmos. Chem. Phys., 11, 8189–8203, 2011.

829 Pandolfi, M., et al.: Effects of sources and meteorology on particulate matter in the Western
830 Mediterranean Basin: An overview of the DAURE campaign, J. Geophys. Res. Atmos., 119,
831 4978–5010, doi:10.1002/2013JD021079, 2014.

832 Pérez, N., Pey, J., Castillo, S., Viana, M., Alastuey, A., and Querol, X.: Interpretation of the
833 variability of levels of regional background aerosols in the Western Mediterranean, Sci. Tot.
834 Environ., 407, 527–540, 2008.

835 Pey, J., Querol, X., and Alastuey, A.: Discriminating the regional and urban contributions in the
836 North-Western Mediterranean: PM levels and composition, Atmos Environ, 44, 1587–96, 2010.

837 Piazzola, J., Sellegri, K., Bourcier, L., Mallet, M., Tedeschi, G., and Missamou, T.: Physicochemical
838 characteristics of aerosols measured in the spring time in the Mediterranean coastal zone, Atmos.
839 Environ., 54, 545-556, 2012.

840 Ramana, M. V., and Ramanathan, V.: Abrupt transition from natural to anthropogenic aerosol
841 radiative forcing: Observation at the ABCMaldives Climate Observatory, J. Geophys. Res., 111,
842 D20207, doi:10.1029/2006JD007063, 2006.

843 Raut, J.-C., and Chazette, P.: Vertical profiles of urban aerosol complex refractive index in the frame
844 of ESQUIF airborne measurements, Atmos. Chem. Phys., 8, 901–919, 2008.Russell, P. B.,
845 Bergstrom, R. W., Shinozuka, Y., Clarke, A. D., DeCarlo, P. F., Jimenez, J. L., Livingston, J. M.,
846 Redemann, J., Dubovik, O., and Strawa, A.: Absorption Angstrom Exponent in AERONET and
847 related data as an indicator of aerosol composition, Atmos. Chem. Phys., 10, 1155–1169,
848 doi:10.5194/acp-10-1155-2010, 2010.

849 Russell, P. B., Bergstrom, R. W., Shinozuka, Y., Clarke, A. D., DeCarlo, P. F., Jimenez, J. L.,
850 Livingston, J. M., Redemann, J., Dubovik, O., and Strawa, A.: Absorption Angstrom Exponent in
851 AERONET and related data as an indicator of aerosol composition, Atmos. Chem. Phys., 10,
852 1155–1169, doi:10.5194/acp-10-1155-2010, 2010.

853 Saha, A., Mallet, M., Roger, J. C., Dubuisson, P., Piazzola, J., and Despiau, S.: One year
854 measurements of aerosol optical properties over an urban coastal site: Effect on local direct
855 radiative forcing, Atmos. Res., *90*, 195-202, 2008.

856 Stamnes K., Tsay, S. C., Wiscombe, W., and Jayaweera, K.: Numerically stable algorithm for
857 discrete-ordinate-method radiative transfer in multiple scattering and emitting layered media,
858 Appl. Opt., 27, 2502–2509, 1988.

859 Stier, P., Schutgens, N. A. J., Bellouin, N., Bian, H., Boucher, O., Chin, M., Ghan, S., Huneeus, N.,
860 Kinne, S., Lin, G., Ma, X., Myhre, G., Penner, J. E., Randles, C. A., Samset, B., Schulz, M.,
861 Takemura, T., Yu, F., Yu, H., and Zhou, C.: Host model uncertainties in aerosol radiative forcing

estimates: results from the AeroCom Prescribed intercomparison study, Atmos. Chem. Phys., 13, 3245-3270, doi:10.5194/acp-13-3245-2013, 2013.

Stohl, A., Hittenberger, M., and Wotawa, G.: Validation of the Lagrangian particle dispersion model Flexpart against large-scale tracer experiment data, Atmos. Environ., 32, 4245–4264, 1998.

Toledano, C., Cachorro, V. E., Berjon, A., de Frutos, A. M., Sorribas, M., de la Morena, B. A., and Goloub, P.: Aerosol optical depth and Ångstrom exponent climatology at El Arenosillo AERONET site (Huelva, Spain), Q. J. Roy. Meteorol. Soc., 133, 795–807, doi:10.1002/qj.54, 2007.

Weingartner, E., Saathof, H., Schnaiter, M., Streit, N., Bitnar, B., and Baltensperger, U.: Absorption of light by soot particles: Determination of the absorption coefficient by means of Aethalometers, J. Aerosol Sci., 34, 1445–1463, 2003.

Tables

Table 1. Summary of information on the SLRs analysed in this study. The SLR location (within the boundary layer or in the free troposphere) was determined based on the boundary layer top height estimated for the closest vertical sounding performed during each flight (see Di Biagio et al., 2015). The sector of origin for sampled air masses was determined based on FLEXPART back-trajectories.

Flight number	SLR_ID	Date	Time start-stop	Altitude (m)	Location	Sector of origin
V19	V19_R1	26/06/2012	11:23-11:38	322	Within the boundary layer	Eastern
V19	V19_R2	26/06/2012	11:44-11:59	897	Within the boundary layer	Eastern
V21	V21_R1	27/06/2012	10:54-11:12	312	Within the boundary layer	Eastern
V21	V21_R2	27/06/2012	11:48-12:04	629	Within the boundary layer	Eastern
V21	V21_R3	27/06/2012	12:05-12:19	311	Within the boundary layer	Western
V22	V22_R1	29/06/2012	7:42-8:01	478	Within the boundary layer	Eastern
V23	V23_R2	29/06/2012	12:05-12:20	319	Within the boundary layer	Open sea
V25	V25_R1	04/07/2012	9:08-9:24	639	Within the boundary layer	Western
V25	V25_R2	04/07/2012	9:32-9:48	2015	Free troposphere	Western
V25	V25_R3	04/07/2012	9:50-10:08	2538	Free troposphere	Western
V26	V26_R2	04/07/2012	17:08-17:25	1877	Free troposphere	Western
V27	V27_R1	06/07/2012	9:28-9:47	164	Within the boundary layer	Open sea
V28	V28_R2	06/07/2012	15:58-16:13	927	Within the boundary layer	Open sea
V30	V30_R1	07/07/2012	14:09-14:28	3498	Free troposphere	Western
V30	V30_R2	07/07/2012	14:51-15:07	549	Within the boundary layer	Open sea
V31	V31_R1	10/07/2012	15:44-16:20	322	Within the boundary layer	Western
V31	V31_R2	10/07/2012	16:31-16:59	954	Within the boundary layer	Western
V32	V32_R1	11/07/2012	12:52-13:13	250	Within the boundary layer	Western
V32	V32_R2	11/07/2012	13:22-13:48	788	Within the boundary layer	Western
V32	V32_R3	11/07/2012	14:02-14:12	336	Within the boundary layer	Western
V32	V32_R4	11/07/2012	14:18-14:35	802	Within the boundary layer	Western

912   **Table 2.** Summary of the aerosol in situ measurements on the ATR-42 during the TRAQA

913   campaign. Details on the data treatment and uncertainty estimation for the different instruments are

914   provided in Sect. 2.

915

916

Property measured	Instrument	Location on aircraft	Flow rate (l min⁻¹)	Time resolution	Size range	Sensitivity or uncertainty	Comments
Aerosol number concentration	Condensation Particle Counter (CPC 3775)	in the cabin behind AVIRAD inlet	1.5	5 sec	$0.004 - 3$ μm	±10% (concentration)	
Aerosol size distribution	Passive cavity aerosol spectrometer probe (PCASP 100x)	aircraft fuselage, left side before the wing	0.06	1 sec	Nominally $0.1 - 3.0$ μm Corrected for refractive index $0.10 - 4.47$ μm	<±25% (diameter optical to geometric conversion) ±15% (concentration) (e.g., Highwood et al., 2012)	Aerosol concentration underestimated by 50% between 0.4 and 1.0 μm
	GRIMM 1.129	in the cabin behind AVIRAD inlet	1.3	6 sec	Nominally $0.3 - 32$ μm Corrected for refractive index $0.28 - 65.80$ μm (AVIRAD 50% cut-off efficiency at ~12 μm diameter)	<±25% (diameter optical to geometric conversion) ±10% (concentration)	Data not available >350 m
Dry aerosol scattering coefficient σ_s (450, 550, 700 nm)	TSI 3563 integrating nephelometer	in the cabin behind AVIRAD inlet	30	6 sec	50% cut-off efficiency at ~12 μm diameter	<±10% for σ_s at 450, 550, and 700 nm	
Aerosol absorption coefficient (σ_a) (370, 470, 520, 590, 660, 880, 950 nm)	Magee AE31 aethalometer	in the cabin behind AVIRAD inlet	13	2 min	50% cut-off efficiency at ~12 μm diameter	11-70% variable at the different wavelengths	Data available only for 60% of SLRs

917

918

919

920

Table 3. Lognormal mode parameters of the measured aerosol size distribution (total aerosol number concentration, N_{tot}, median diameter, D_g, and geometric standard deviation, σ_g). Data corresponds to SLRs below ~350 m altitude. Diameters are given in microns and number concentrations refer to ambient conditions.

		Mode 1	Mode 2	Mode 3	Mode 4	Mode 5	Mode 6	Mode 7
V19_R1	N_{tot}	498	160	12	4.0	1.6	0.04	
	D_g	0.13	0.24	0.38	0.61	1.55	4.85	
	σ_g	1.19	1.16	1.17	1.29	1.60	1.45	
V21_R1	N_{tot}	600	210	2.0	5.5	0.65		
	D_g	0.13	0.24	0.37	0.48	1.35		
	σ_g	1.20	1.17	1.15	1.40	1.62		
V21_R3	N_{tot}	600	195	2.7	3.0	0.50	0.01	
	D_g	0.13	0.23	0.35	0.51	1.45	4.50	
	σ_g	1.19	1.21	1.18	1.38	1.66	1.41	
V23_R2	N_{tot}	660	195	2.0	3.2	0.80	0.02	
	D_g	0.13	0.23	0.37	0.53	1.45	5.69	
	σ_g	1.19	1.16	1.16	1.37	1.65	1.25	
V27_R1	N_{tot}	930	264	2.5	5.2	0.70	0.04	0.004
	D_g	0.13	0.23	0.37	0.48	1.30	3. 50	8.20
	σ_g	1.19	1.20	1.18	1.40	1.68	1.12	1.26
V31_R1	N_{tot}	482	278	48	2.7	0.55	0.01	
	D_g	0.14	0.24	0.35	0.54	1.82	7.14	
	σ_g	1.20	1.16	1.17	1.39	1.65	1.17	
V32_R1	N_{tot}	1135	413	55	5.0	0.65	0.01	
	D_g	0.13	0.23	0.37	0.50	1.65	7.30	
	σ_g	1.19	1.18	1.16	1.37	1.66	1.11	
V32_R3	N_{tot}	235	8	8	3.2	0.15	0.02	0.002
	D_g	0.14	0.28	0.28	0.40	1.42	3.29	7.21
	σ_g	1.19	1.16	1.16	1.32	1.68	1.12	1.31

Table 4. Maximum, mean, and minimum of the single scattering albedo considered for radiative transfer calculations. Values are reported at the 7 wavelengths used as inputs in the GAME model.

	330 nm	400 nm	550 nm	670 nm	870 nm	1020 nm	1500 nm
SSA max	0.98	0.98	0.99	0.99	1.00	0.99	0.99
SSA mean	0.93	0.93	0.92	0.91	0.90	0.90	0.89
SSA min	0.88	0.87	0.85	0.85	0.83	0.82	0.80

Figures

Figure 1. Upper panel: geographical position of the different straight levelled runs (SLRs) performed during the TRAQA campaign and analysed in this paper. The label for each point in the figure identifies the flight number and the corresponding SLR: for example V22_R1 indicates the coordinates of the first SLR of flight V22. Lower panel: definition of three different source areas for the various SLRs (see Sect. 3.4 for more details). The Western sector includes trajectories coming from the Atlantic Ocean and travelling over France or northern Spain before reaching the Western basin; the Eastern sector includes air mass trajectories from continental Europe that have travelled over northern Italy-Po Valley before entering the basin; and the Open sea sector consists of trajectories which have experienced at least 2 days of subsidence over the sea in the Western basin.
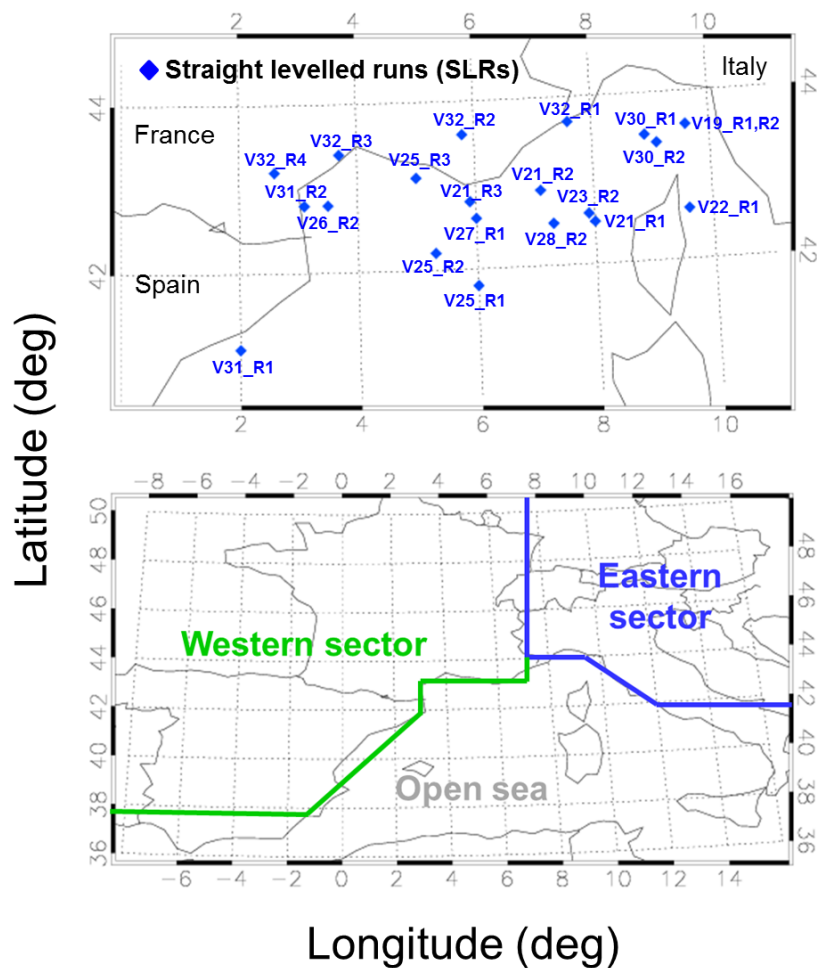
951 **Figure 2.** Flowchart of the size distribution and refractive index retrieval procedure. Further details

952 are provided in Sect. 3.2.

953
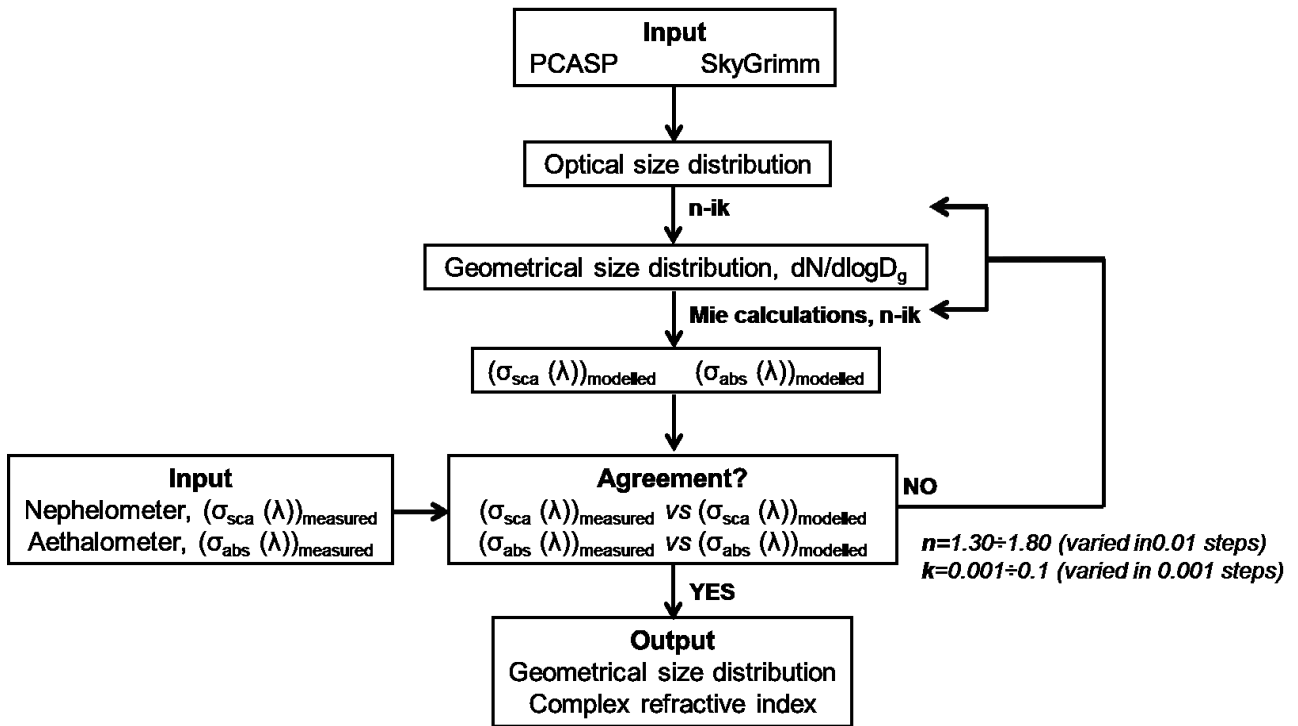
954
955
956
957
958
959
960
961
962
963
964
965
966
967
968
969
970

Figure 3. Averages over the different TRAQA straight levelled runs (SLRs) of the measured: altitude, spectral scattering coefficient (σ_s; 450, 550, and 700 nm), scattering Ångström exponent (SAE), spectral absorption coefficient (σ_{abs}; 370, 470, 520, 590, 660, 880, and 950 nm), absorption Ångström exponent (AAE), ozone enhancement factor ($\Delta O_3/\Delta CO$) and ultrafine-to-accumulation ratio (dN_{UFP}/dN_{Acc}). Uncertainties indicate the 1-σ standard deviation. The x-axis indicates the flight number (19 to 32 for flights V019 to V032); each point for the same flight number represents a different SLR.
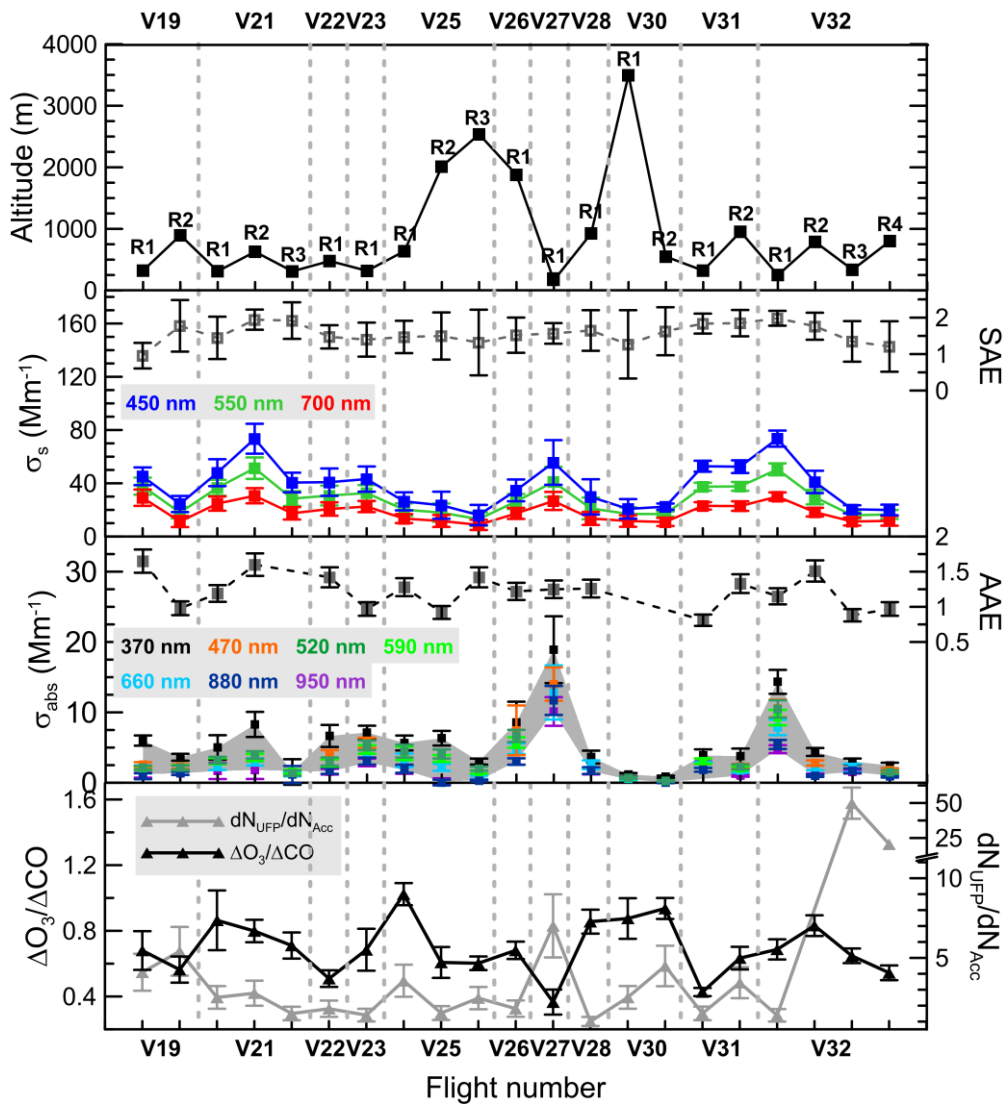
Figure 4. Number size distributions (left panel) and volume size distributions (right panel) measured over the different SLRs for the TRAQA flights. Data corresponds to measurements performed within the boundary layer at altitudes <350 m (V19_R1, V21_R1, V21_R3, V23_R2, V27_R1, V31_R1, V32_R1, V32_R3). Data are separated based on the different air mass origin (Western sector, Eastern sector, and Open sea). Concentrations are given at ambient conditions. Grey shading represents minimum and maximum measured values, while the black curve is the average size. Measurement uncertainties are also reported for the average curve.
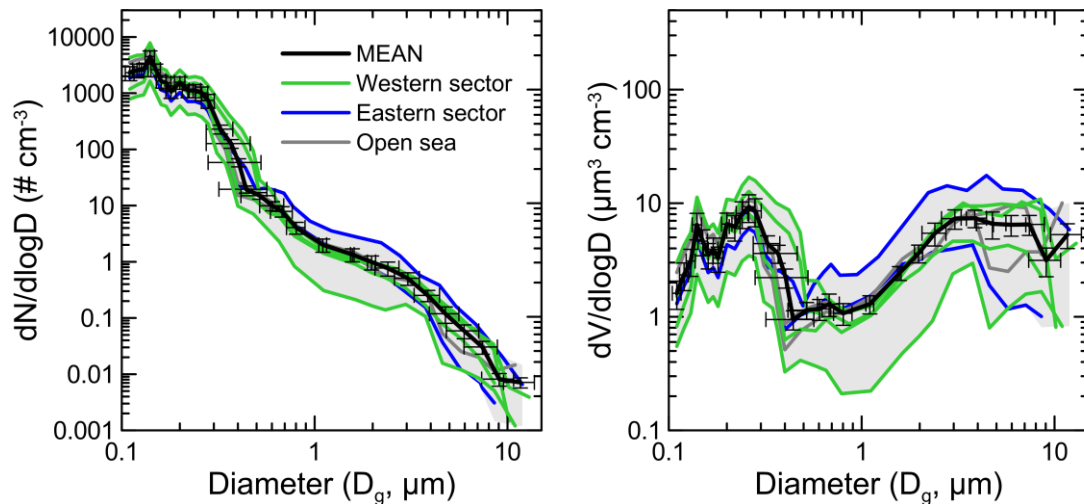
Figure 5. Spectral single scattering albedo at seven wavelengths between 370 and 950 nm calculated from nephelometer and aethalometer measurements for the different SLRs within pollution layers. Data are separated based on the different air mass origin (Western sector, Eastern sector, and Open sea).
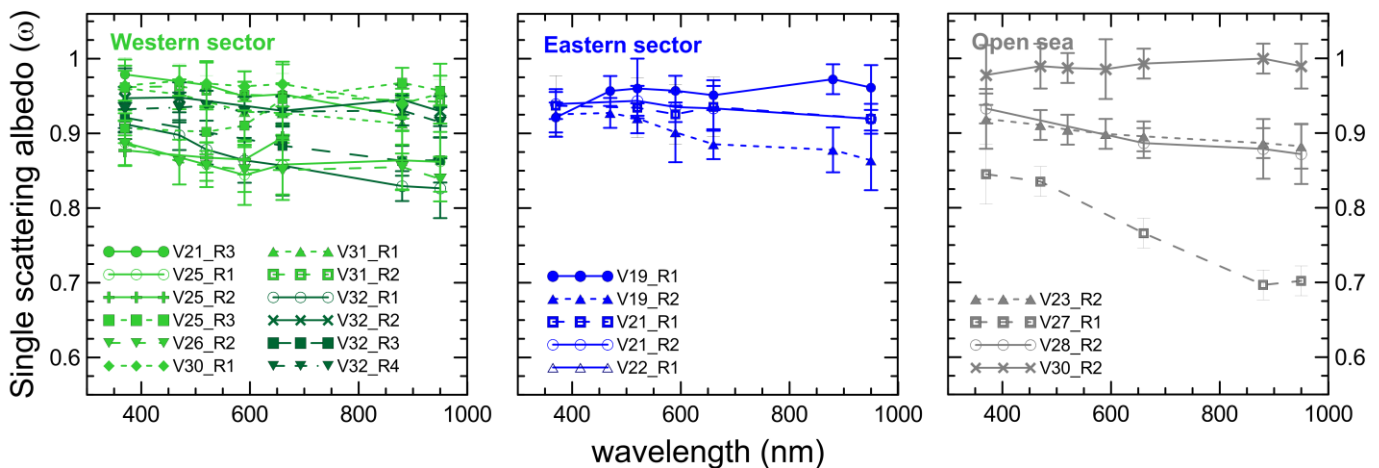
Figure 6. Single scattering albedo (370, 660, and 950 nm), ozone enhancement factor ($\Delta O_3/\Delta CO$), ultrafine-to-accumulation ratio (dN_{UFP}/dN_{Acc}), and scattering (SAE) and absorption Ångström exponent (AAE) versus height for all analysed SLRs cases. Uncertainties on measured and retrieved quantities (horizontal bars) are also shown in the plots.
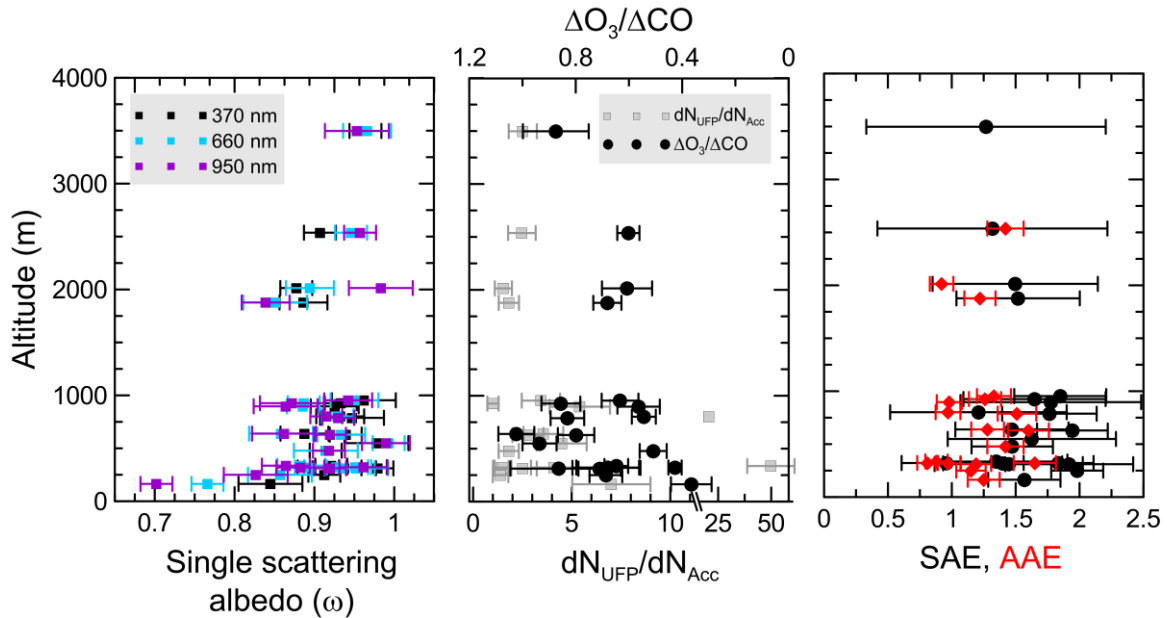
Figure 7. Comparison of the aerosol scattering (σ_s, left panel) and absorption (σ_{abs}, right panel) coefficients measured by the nephelometer and the aethalometer and calculated from measured size distribution data with Mie theory. Data are given at ambient conditions. Uncertainties on the measured (horizontal bars) scattering and absorption coefficients are also shown in the plots.
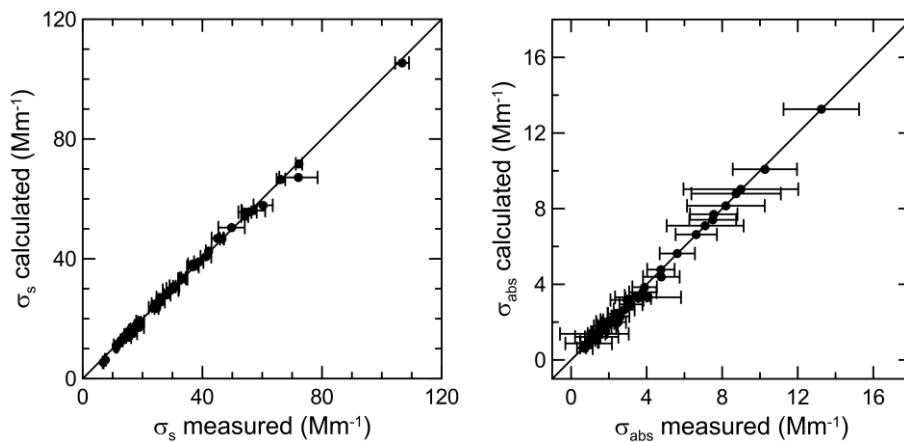
1018 **Figure 8.** Spectral real (n, left panel) and imaginary (k, right panel) parts of the complex refractive

1019 index obtained by optical closure for the 8 selected case studies. For sake of clarity, uncertainties on

1020 n and k are not reported in the plot. The values of the single scattering albedo measured at 370 and

1021 950 nm for the different cases are reported in the legend. The spectral real and imaginary parts of

1022 the complex refractive index as obtained from the Optical Properties of Aerosols and Clouds

1023 (OPAC, Hess et al., 1998) database for insoluble, water soluble, soot and sea salt components are

1024 also reported in the plot. These components are used in OPAC to model continental polluted,

1025 continental rural, urban, and maritime polluted aerosols.

1026
1027
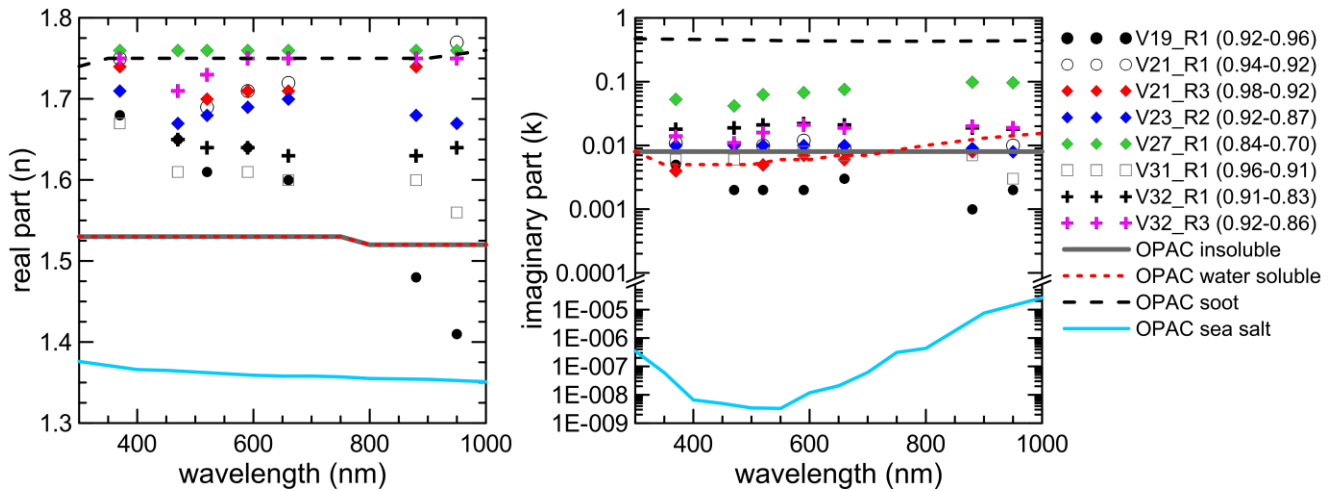
1028
1029
1030
1031
1032
1033
1034
1035
1036
1037
1038
1039
1040
1041
1042
1043

Figure 9. Spectral single scattering albedo plotted against the real (left panel) and the imaginary (right panel) parts of the complex refractive index. The results of the linear fit between ω and k are reported in the legend. The fits are performed for the whole ω-k dataset, and also eliminating the data in correspondence of V27_R1, for which the largest values of k were observed.
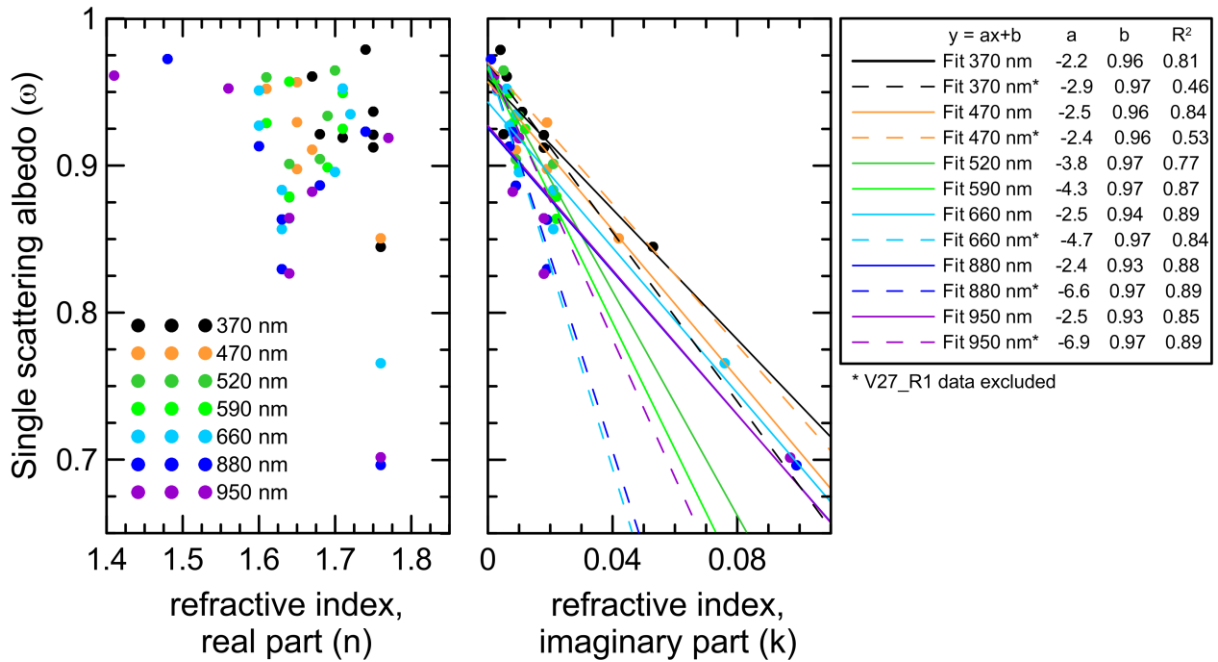
Figure 10. Aerosol shortwave forcing efficiency at 60° solar zenith angle calculated at the surface, TOA, and within the atmosphere for the maximum, mean, and minimum of the single scattering albedo (ω) observed in this study (Table 4).